ADVANCED QUANTUM TECHNOLOGIES
www.advquantumtech.com

Quantum Ghost Imaging by Sparse Spatial Mode Reconstruction

*Fazilah Nothlawala, Chané Moodley, Neelan Gounden, Isaac Nape, and Andrew Forbes**

In a conventional quantum imaging experiment, the image of the object is retrieved directly with single photon camera technology, or computationally with a single-pixel detector and pixelated projective masks. In all these approaches, the resolution of the image is dictated by the pixel resolution of the detection devices. In this paper, the traditional spatial basis of pixels is replaced with spatial modes, exploiting their unique features to enhance image fidelity and resolution and improve reconstruction accuracy through modal sparsity. This approach can be used even when the modes are not orthogonal, demonstrating the principle with highly efficient phase-only approximations to the modal basis. By numerical simulation and experimental analysis, the advantages of this approach are illustrated, which include faster convergence to the object, with higher signals and fidelity, which are demonstrated with an order of magnitude less masks than conventional approaches for the same fidelity in outcome. Unlike the basis of pixels, the resolution of the image is not dictated by the resolution of the detectors, opening a path to high-resolution quantum imaging of complex objects.

1. Introduction

Quantum ghost imaging[1–5] is a specific realization of quantum imaging,[6–8] where correlated photon pairs form an image of an object despite neither having any object information. Beyond the traditional bi-photon entangled pair as a resource, it has been used with entanglement-swapped photons,[9] with Hong–Ou–Mandel interference[10] and recently allowed for 3D imaging by direct time of flight (ToF) methods.[11] An advantage of quantum ghost imaging is the low photon intensities inherent to quantum optics experiments, enabling the reconstruction of images with a higher signal-to-noise ratio (SNR) and better visibility compared to classical ghost imaging.[12,13] In particular, quantum ghost imaging has proven valuable in biological imaging applications where minimizing photodamage to light-sensitive matter is beneficial,[14] and was recently shown to produce high-quality images of biological organisms through spatial and polarization entanglement,[15] achieving higher resolution and SNR than classical techniques. Moreover, a unique variation of quantum ghost imaging demonstrates exceptional capabilities by generating non-degenerate signals and idler photons. This approach enables imaging at specific wavelengths without requiring a camera sensitive to that wavelength, instead utilizing a more sensitive, less noisy, or cost-effective camera for detection.[16]

Initially, ghost imaging experiments accomplished spatially resolved detection by a physically moving single-pixel detector, which scanned a transverse plane.[17] Later advancements replaced mechanical scanning to form an image of the object with a series of pixelated, projective masks, e.g., Hadamard masks.[18] Consequently, the resolution of the produced image was directly determined by the resolution of the detectors or masks employed[19] via their pixel size and number of pixels, N. Achieving high-resolution images with projective masks require using high-resolution mask sets, where the number of pixel masks in the set scales quadratically with the resolution, i.e., as N^2 for a mask resolution of $N \times N$.[20] Since imaging techniques using a bucket detector rely on a single value per measurement, a large number of measurements (N^2) are required for a complete image reconstruction. Thus, efforts to enhance the resolution of the reconstructed image inherently demand a greater number of measurements, leading to longer image acquisition times[5,21–23] and techniques such as smart photon-number-resolving detection[24] and super-resolving neural networks have been developed to achieve high-resolution images in less time.[23] An alternative to projective masks is the use of detector arrays with single-photon sensitivity, such as intensified CCDs (ICCDs), which enable high-speed quantum imaging with few photons.[25,26] In this approach, the camera is triggered by the imaging photon which has to incur an image-preserving delay to fit within the camera's measurement time frame.[25,27] This is one of the main disadvantages of this scheme, as maintaining the spatial correlations of the photon pairs demands precise imaging of the idler photons onto the object in the same plane as the photons at the camera. Moreover, in all these approaches, the image resolution is limited by the pixel resolution of the detection devices, and in the former case,

F. Nothlawala, C. Moodley, N. Gounden, I. Nape, A. Forbes
Structured Light Laboratory, School of Physics
University of the Witwatersrand
Johannesburg 2000, South Africa
E-mail: andrew.forbes@wits.ac.za

The ORCID identification number(s) for the author(s) of this article can be found under https://doi.org/10.1002/qute.202400577

DOI: 10.1002/qute.202400577

requires an increased number of measurements to achieve high-resolution imaging.

Rather than using the position basis of pixels, "space," one can instead consider using "spatial modes," e.g., the exotic forms of structured light.[28–33] This would form a modal basis and has been used extensively in classically structured light to unravel the properties of light,[34–39] as well as in probing high-dimensional structured quantum states.[40–44] Of key relevance to this discussion is that the modal basis is usually a continuous function rather than a pixellated function, and thus has the ability to reconstruct at any desired spatial resolution, as has been demonstrated in the classical wavefront, phase and intensity reconstructions.[45] It has been shown to achieve high resolution images in optical image reconstruction on a modal basis tailored to the symmetries of the object[46] and to infer step heights with nanometer resolution.[47] It has recently found its way into resolving distances beyond the diffraction limit,[48] applied to classical[49] and quantum[50] sources, but not yet in quantum ghost imaging of complex objects.

Here we replace the traditional spatial basis of pixels with spatial modes and demonstrate quantum ghost imaging of complex objects with high spatial resolution (less pixelation) and good fidelity (close to the object in key properties). Unlike the basis of pixels, the basis modes are continuous functions with a spatial resolution that resides computationally in the computer memory, so that the object can be reconstructed to high spatial resolution. We show that the approach can be used even when the modal basis is not orthogonal, demonstrating the principle with highly efficient phase-only approximations to the modal basis, thus by-passing the lossy complex amplitude modulation usually required for spatial modes. We deploy a modal sparsity technique and show that this can dramatically minimize the number of measurements needed. The result is higher fidelity, higher spatial resolution quantum ghost images with reduced measurements by exploiting modal sparsity. Throughout the study, we use the Hermite–Gaussian (HG) basis as an example, but stress that the approach can be deployed with any spatial basis of choice, highlighting that the optimal choice will likely be based on symmetry considerations of both the object and basis.

2. Concept

The concept of image reconstruction using projective masks, the goal of digital ghost imaging, is analogous to the modal decomposition of complex structured light, namely, the idea that any complex optical field function can be described by a complete and orthonormal set of basis modes, where the function may represent a physical or digital object. Importantly, the features of the object are encoded into the internal degrees of freedom of the photon fields, namely, the amplitude and phase. This means that an object's image can be described as a linear combination of the optical field functions that comprise such a basis following

$$O(x,y) = \sum_{j=0}^{N-1} c_j M_j(x,y) \tag{1}$$

where $O(x,y)$ is the reconstructed image of an object based on the sum of basis functions $M_j(x,y)$ with weighting coefficients c_j normalized such that $\sum |c_j|^2 = 1$, i.e., the modal powers add to 100% (the trace is 1 in quantum language). If the basis elements are orthonormal then the complex weighting coefficients can be found from $c_j = |c_j| \exp(i\theta_j) = \langle O(x,y) | M_j(x,y) \rangle$.[34] This concept is illustrated graphically in **Figure 1a**, where an amplitude object (flower) is reconstructed from a sum of Hadamard basis elements (top row) and Hermite–Gaussian basis elements (bottom row). The latter is the basis of spatial modes, where the mode set can be selected based on the symmetry of the object.

However, the above construction relies on the ability to extract both the phase (θ_j) and amplitudes ($|c_j|$). Quantum ghost imaging with projective masks has the inbuilt ability to infer phase[51] using projective measurements constructed in a similar fashion to wavefront reconstruction approaches. To extract modal phases (θ_j) it is useful to measure not only directly in the modal basis elements but also in superpositions of these modes,[34]

$$T_j(x,y) = \frac{M_j(x,y) + M_r(x,y)}{\sqrt{2}} \tag{2}$$

using the j^{th} ($M_j(x,y)$) basis mode and the r^{th} ($M_r(x,y)$) reference mode. This mimics traditional ghost imaging with Hadamard basis modes where the projective amplitude masks are rescaled to have amplitudes proportional to 0 and 1 and are computed by superposing each Hadamard basis state with the uniform superposition of pixels, i.e., corresponding to the first basis state ($r = 0$). Given these projections, the image is then reconstructed from[19]

$$\tilde{O}(x,y) = \sum_{j=0}^{N-1} (a_j - \langle a_j \rangle_N) M_j(x,y) \tag{3}$$

where $a_j = |\langle O | T_j \rangle|^2$ and $\langle a_j \rangle_N$ is the ensemble average over all N measurements. Because, $a_j = \frac{1}{2}|c_j|^2 + \frac{1}{2}|c_r|^2 + |c_j||c_r|\cos(\theta_j - \theta_r)$ the resulting image is given by

$$\tilde{O}(x,y) \propto \sum_{j=0}^{N-1} |c_j||c_r| \cos\left(\theta j - \theta_r\right) M_j(x,y) \approx |c_r| \mathrm{Re}\left[O(x,y) e^{-i\theta_r}\right] \tag{4}$$

producing the real part of the reconstructed image up to a phase, θ_r, corresponding to the phase for the chosen reference mode.

A common mode set is that of orbital angular momentum (OAM), but OAM is a 1D basis and thus not suitable for 2D imaging of objects, although it has proven useful to extract information of features from objects.[52,53] Instead, to illustrate this concept, we will use Hermite–Gaussian (HG) modes which have Cartesian symmetry, though the results are equatable to other modes in other symmetries, e.g., Laguerre–Gaussian modes in cylindrical symmetry, which have been successfully applied to classical imaging.[46] Our HG modes are defined as,

$$M_i(x,y) \equiv \mathrm{HG}_{nm}(x,y) = \sqrt{\frac{2}{\pi w_0^2 n! m! 2^{m+n-1}}} H_n\left(\frac{\sqrt{2}x}{w_0}\right) \times H_m\left(\frac{\sqrt{2}y}{w_0}\right) \exp\left(-\frac{x^2+y^2}{w_0^2}\right) \tag{5}$$

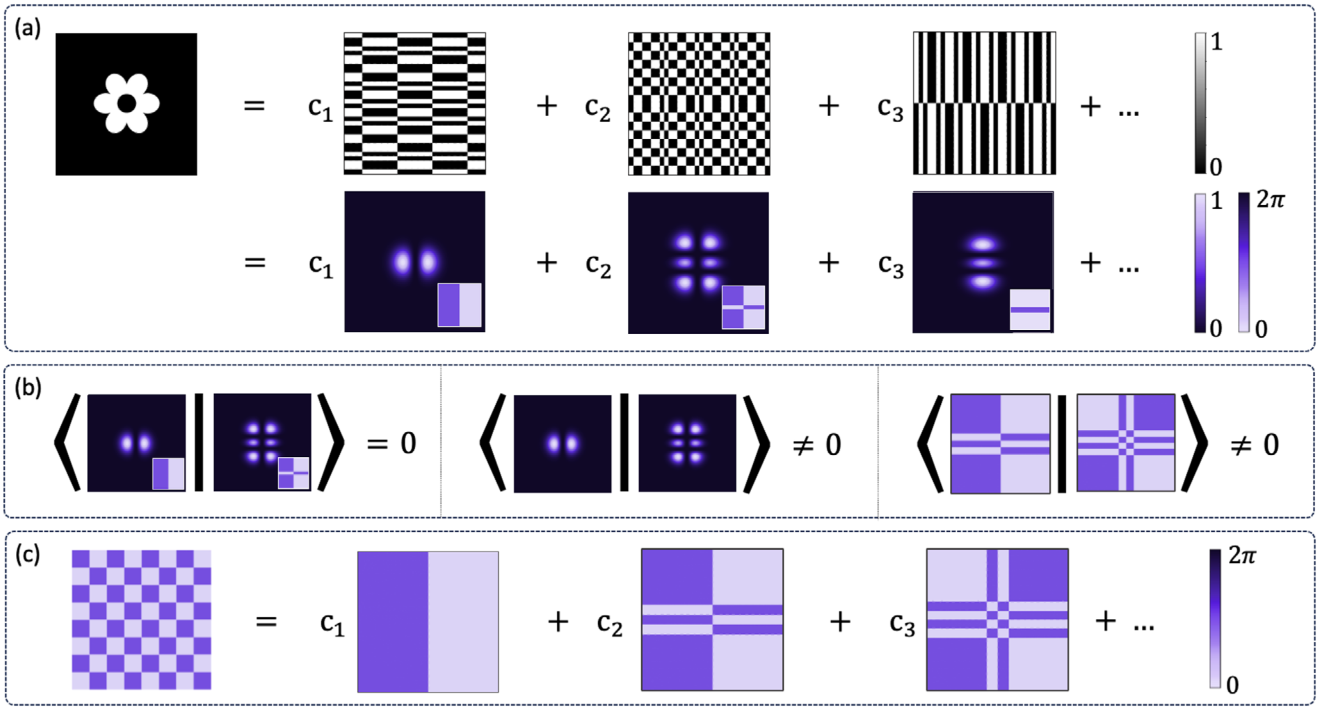

Figure 1. a) Reconstruction of an arbitrary amplitude object by a linear combination of basis functions, Hadamard and Hermite-Gauss shown as examples, respectively. b) Orthogonality relations for HG modes dictate that they are orthogonal as full complex fields (left) but not as amplitude-only (middle) or phase-only (right) functions. c) Nevertheless, phase objects can be reconstructed employing phase-only HG masks for low-loss object reconstruction.

where n and m are mode indices, and $H_n(\cdot)$ and $H_m(\cdot)$ are Hermite polynomials of order n and m, respectively. Here w_0 is the embedded Gaussian beam size and the function is defined at the $z = 0$ plane. Examples of the intensity and phase of various HG modes are shown in **Figure 2** for increasing n and m indices, each increasing the number of intensity lobes in the horizontal and vertical directions, respectively. These modes are solutions to the wave equation in Cartesian co-ordinates and as such are Fourier transforms of themselves. The HG modes also form an orthogonal basis, as shown in Figure 1b. This orthogonality is ensured by both the Hermite polynomials and their Gaussian weighting factor, i.e.,

$$\int_{-\infty}^{\infty} H_n(x) H_k(x)\, e^{-x^2} = 2^n n! \sqrt{\pi} \delta_{n,k} \tag{6}$$

It is however broken if the spatial mode is approximated by amplitude-only or phase-only functions, shown in the middle and far right panels of Figure 1b.

Although the HG modes provide a complete and orthonormal basis, they require both amplitude and phase modulation in their implementation, the former resulting in a lossy process. In a quantum optics experiment with inherent low-light levels, it is essential to mitigate such losses. One approach is to use a phase-only approximation to the spatial mode basis, allowing for efficient quantum detection. In the example of the HG modes, this results in a binary phase structure, where the phase emerges from the property of the Hermite polynomials: a series of phase jumps between 0 and π across the transverse beam profile, as seen in Figure 1c. Mathematically, this can be written as

$$\mathrm{HG}_{nm}^{\mathrm{Phase}}(x, y) = \mathrm{sign}[\mathrm{Re}(\mathrm{HG}_{nm}(x, y))] \tag{7}$$

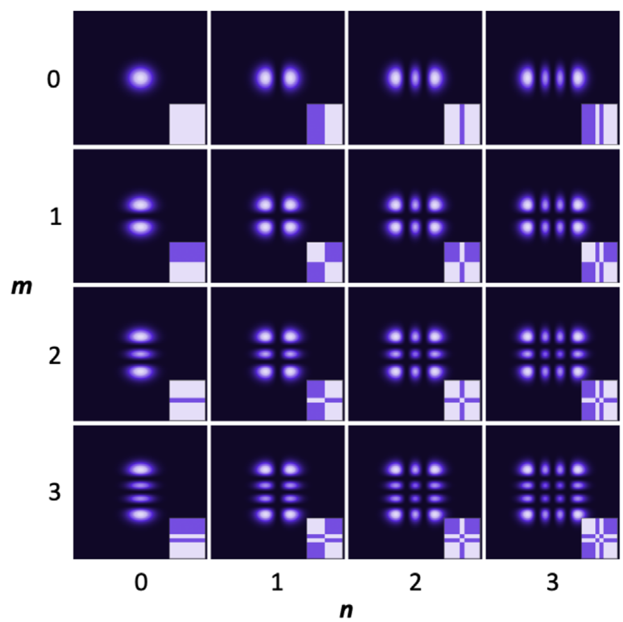

Figure 2. Intensity and corresponding phase profiles (inset) of Hermite-Gaussian (HG) modes from HG_{00} to HG_{44}, with mode index n increasing from left to right and m increasing from top to bottom. As the mode index increases so does the mode size.

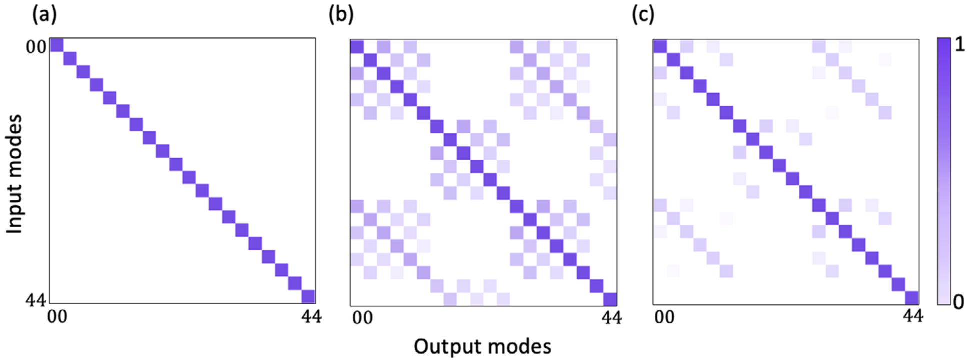

Figure 3. Simulated cross-talk matrices illustrating the orthogonality of a) Full HG modes, b) Phase-only HG modes and c) Phase-only HG modes with a Gaussian envelope, using HG modes ranging from HG_{00} to HG_{44}.

We explore this orthogonality in **Figure 3**. The full HG basis functions have no cross-talk as they are inherently orthogonal, as shown in Figure 3a for HG modes ranging from HG_{00} to HG_{44}. The phase-only approximation to the HG basis, while in principle lossless, comes at the penalty of orthogonality of the basis functions, as shown in Figure 3b. The orthogonality of the full Hermite–Gauss modes relies on the specific properties of the Hermite polynomials with respect to their weighting function, which are lost when only considering their sign in the phase-only representation. However, the incorporation of a Gaussian envelope in this phase-only representation preserves a degree of orthogonality, as demonstrated in the corresponding cross-talk matrix in Figure 3c. This is highly convenient as in most spatial mode experiments, light is coupled into a single mode fiber, providing the necessary Gaussian envelope "for free." Thus, the experimental representation of the phase-only HG modes includes the Gaussian envelope, resulting in a set of phase-only modes that partially preserve the orthogonality of the original basis.

To demonstrate the feasibility of the modal basis, we show numerical image reconstructions in **Figure 4a**, where an amplitude object (flower) is reconstructed using the traditional Hadamard mask set, and complex-amplitude HG modes. In this simulation no noise is added and ideal conditions are assumed, but we return to the issue of practical considerations shortly. The amplitude image reconstruction with the HG modal basis used complex coefficients $c_j = |c_j|e^{i\theta_j}$, to produce a higher quality image compared to the Hadamard reconstruction, which extracted real coefficients $|c_j|^2$ to form an image. The Hadamard masks were set to a resolution of 64×64, and stopped at 4096 measurements. With an equal number of HG modes, the HG reconstruction qualitatively outperforms the Hadamard set. Figure 4b shows the complete reconstruction of a phase object using phase-only Hadamard and HG masks. Our simulations show that the object's phase is successfully recovered, using efficient, phase-only approximations to the reconstruction bases.

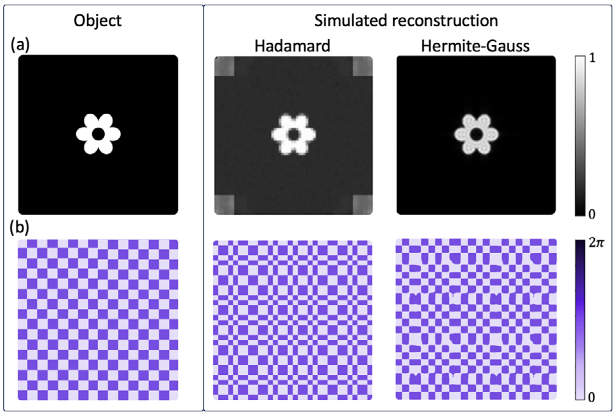

Figure 4. Simulated image reconstructions for a) an amplitude object using Hadamard amplitude masks and complex amplitude HG masks and b) repeating phase chess using Hadamard phase masks and HG masks.

Usually non-orthogonal basis sets require significantly more projective masks to achieve a general image reconstruction as opposed to the N^2 masks needed for an orthogonal basis set, e.g., $2N^2$ projective masks are required for random masks of size $N \times N$, in comparison to N^2 masks for the Hadamard basis (see ref. [19] for a tutorial on the topic). The benefit of the spatial basis is that it is known that complex reconstructions of optical fields are possible with very few modes,[54] facilitated by the fact that the reconstruction resolution is embedded into the basis itself. This naturally leads to the notion of modal sparsity[55] in our quantum implementation, where modal contributions of low power are filtered out while retaining meaningful information for image reconstruction.[56] We observe that when the image reconstruction data is modally sparse, most of the object information is held by specific modes, and by focusing on these modes in the reconstruction process, we can achieve high-fidelity images in a shorter time.

3. Experimental Implementation

A schematic diagram of the degenerate quantum ghost imaging experiment employed to obtain our results is shown in **Figure 5a**. Light from a diode laser of wavelength $\lambda = 405$ nm, and power 100 mW was sent to a temperature controlled Periodically Poled Potassium Titanyl Phosphate (PPKTP) non-linear crystal of length 2 mm. The PPKTP crystal was phase-matched for degenerate spontaneous parametric down-conversion (SPDC). From the SPDC parameters, we determine the correlation radius of our SPDC distribution to be 60 μm,[57] for a SPDC beam radius of $\omega_R = 3$ mm, both as measured at the plane of the spatial light modulators (SLMs). The number of modes available for imaging is obtained by dividing out the area of the photon correlations

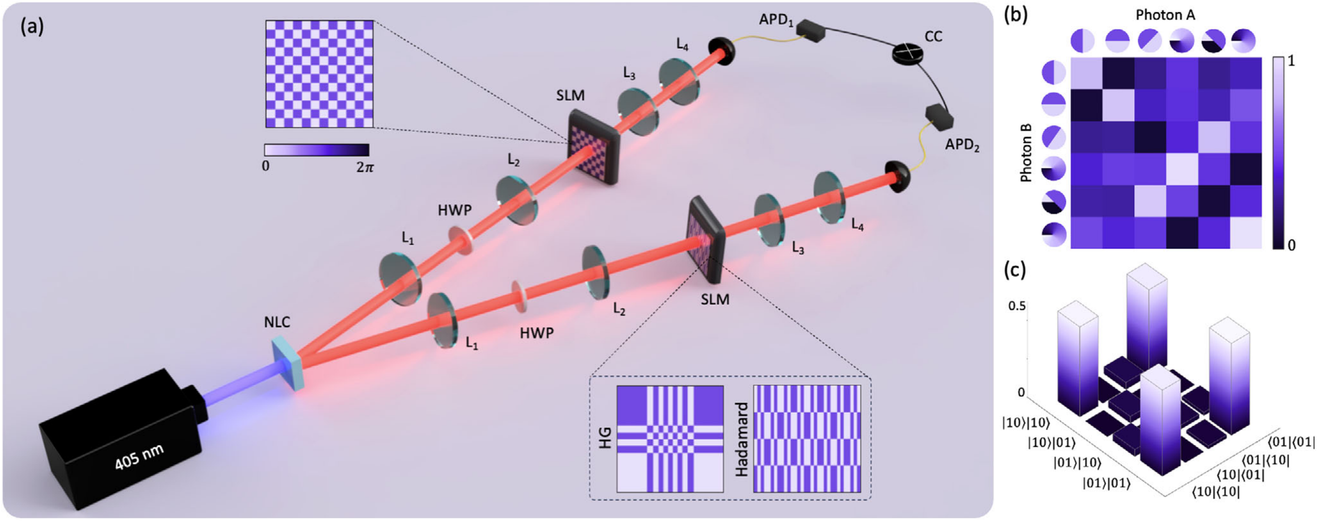

Figure 5. a) Schematic diagram of the degenerate quantum ghost imaging setup of non-collinear SPDC that was employed for image reconstruction. The non-collinear SPDC is produced using the non-linear crystal (NLC) and each photon path is sent to an SLM. One SLM displays the object and the other displays a spatial mask. Each photon path is coupled to a single-mode fiber, connected to an APD for detection. The photons that are detected in coincidence are registered by a coincidence counting device (CC). b) A two-qubit quantum state tomography with HG modes, HG_{10} and HG_{01} is shown, where the projected state of each photon in the entangled pair is indicated by its phase map. The color of each box represents the normalized coincidence counts for a given set of projections on the two-photon state. c) Using the tomographic data, the density matrix is computed, and its real component is shown.

from that of the SPDC beam,[58] and in this experiment has an upper bound of ~2500 modes. The temperature of the crystal was optimized to 57 °C to obtain non-collinear entangled photons of wavelength, $\lambda = 810$ nm (via SPDC of Type I), so that the down-converted photons propagated off-axis with regards to the pump in two spatially separated paths, namely, the object arm and the image arm. The object arm consisted of an SLM that displayed the digital object to be imaged while the SLM in the image arm displayed the projective masks. In addition to displaying object and mask holograms, a blazed-grating hologram was displayed on each SLM to separate the first diffraction order of the light from its zeroth order. The photons from each arm were then coupled to optical single-mode fibers (SMFs), which were connected to avalanche photo-diodes (APDs) for photon detection. The photon counting device (CC) measured the coincidences within a 3 ns detection window, detecting a maximum coincidence count rate of ~9000 counts per second.

We test for the presence of entanglement in our ghost imaging setup prior to taking our imaging results. We tested for the entangled nature of OAM states generated in SPDC by performing projective measurements on our quantum state by displaying the appropriate holograms on the SLMs in each arm. The measurements are performed to demonstrate a violation of the Clauser–Horne–Shimony–Holt (CHSH) Bell inequality. Our results demonstrate a violation of the Bell inequality with a Bell parameter of $S = 2.72 \pm 0.003$ for the $l = \pm 2$ OAM subspace. Furthermore, to confirm the presence of entanglement a full quantum state tomography (QST) was performed for HG modes, HG_{10} and HG_{01}, with tomographic measurements shown in Figure 5b. Using the tomographic data, the density matrix was computed, and its real part is shown in Figure 5c. For our density matrix we obtain a fidelity of $F = 0.962$ with respective to a maximally entangled state, a concurrence of $C = 0.927$, and a linear entropy of $S_L = 0.061$, all confirming the strong presence of entanglement in our experiment.

4. Results and Discussion

We start with phase objects, with the results shown in **Figure 6**. In Figure 6a, we show reconstruction results for a complex letter "G" object. This object lacks Cartesian symmetry and is therefore considered a "complex" object from the perspective of HG modes, which are inherently Cartesian. Using a modal sum of 1024 phase-only HG modes with a beam waist $\omega_{HG} = 0.8$ mm, the object is reconstructed effectively (with a runtime of 1 h). The results are expressed in both phase-only and full complex amplitude HG basis representations, showcasing the versatility of these modes in capturing the object's structure despite its complexity. In Figure 6b we select an example that has more apparent Cartesian symmetry, the letter "H," but yet performs poorly with the HG modal approach (by design). We use this example to highlight the interplay between experimental parameter choices and the choice of the modal basis parameters. Simulated results are presented for varying beam waists of the modes, demonstrating that smaller HG mode beam waists correspond to better reconstructions. However, in the experimental setup, the spatial resolution is limited by the SPDC source, which constrains the ability to resolve features smaller than the correlation width. This limitation sets the allowed modal basis radius to a minimum of 0.8 mm - too large for a high-fidelity reconstruction - with experimental and simulated results in good agreement. This emphasizes the point that the modal basis cannot be selected without consideration of the object parameters and the SPDC parameters (as is the case in all quantum imaging experiments).

Next, we acquired results for three different phase objects of Cartesian symmetry, shown in **Figure 7**. The simulated

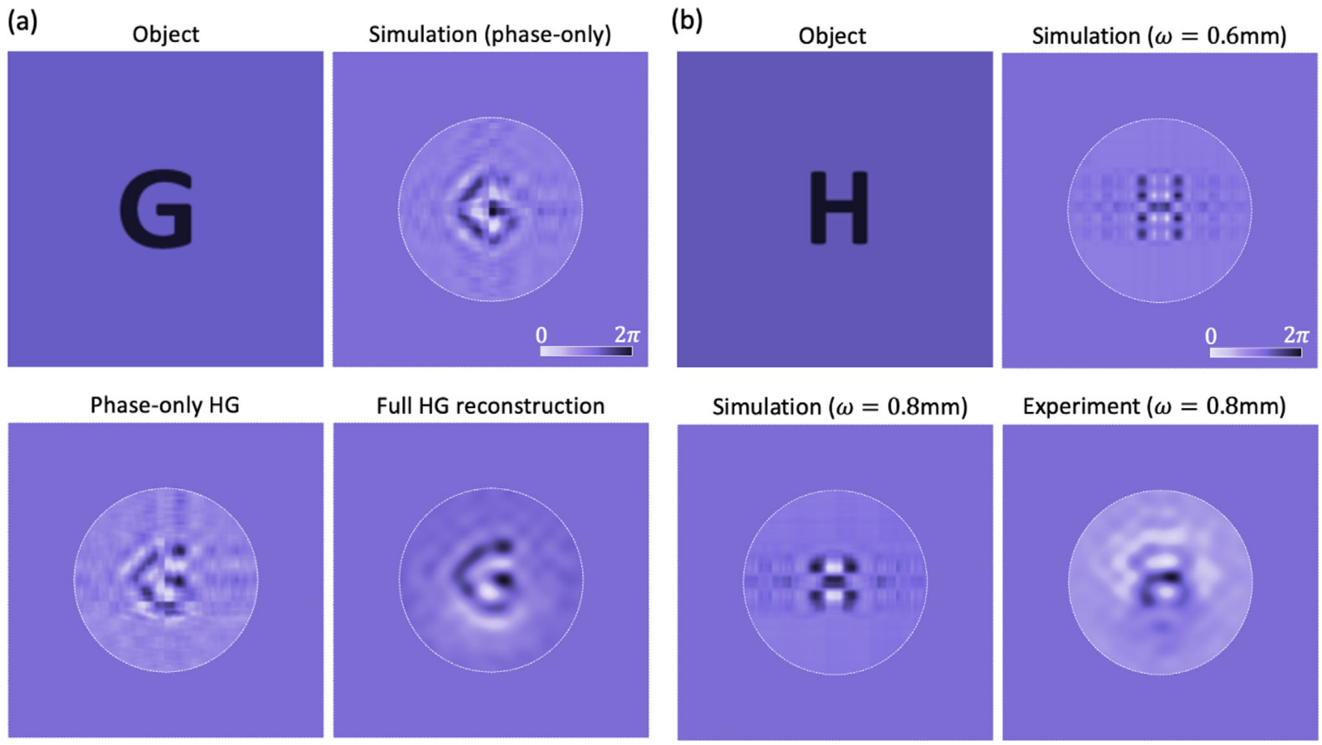

Figure 6. Simulated and experimental reconstruction results for a) the letter G, using a modal sum of 1024 phase-only HG modes and full complex amplitude HG modes, with the experimental results displayed in the lower panel. b) the letter H, showing simulations with a modal radius of 0.6 mm and 0.8 mm, together with the experimental image at 0.8 mm. All images were reconstructed with 1024 modes. Here, the outer area of the circle indicates the region in which noise was suppressed due to lack of SPDC signal.

quantum image reconstructions, employing Hermite–Gauss and Hadamard masks, closely align with the corresponding experimental image reconstructions. This is shown in Figure 7, where the complete phase of the object is recovered for both the Hadamard and Hermite–Gauss basis sets, showing excellent agreement with the simulated reconstruction.

The high-fidelity reconstructions in this case have benefited from modal sparsity. In **Figures** 8 and 9, the graphs depict the normalized modal power contributions for each of the modes in our mask sets, showing distinct power peaks for specific modes. This implies that these modes have the largest overlap with our objects, and most of the object information is held by these modes. We exploit this modal sparsity by filtering out the low-power contributions and retrieving high-fidelity reconstructions of our objects. This is seen in the images in Figures 8 and 9, which show how our initial noisy, raw experimental images are transformed into higher fidelity image reconstructions through increased modal filtering. We start off with no filtering, considering all modal contributions in our reconstruction, shown in the first image of this panel. Here, we see a pattern present for the Hadamard case but none for the HG case. In the next image, we reconstruct the image after 50% modal filtering, i.e., excluding modal contributions that are below 50% of the total modal power from the reconstruction. This reduces the noise from lower order contributions in our images, showing a smoother reconstruction for both sets, but specifically for the HG set which has an immediate jump in fidelity (also seen in **Figure** 10). Lastly, we see perfect reconstructions for both basis sets in the last case, with 90% modal filtering (excluding modal contributions that are below 90% of the total modal power).

The Hadamard basis requires N^2 measurements for a complete reconstruction, and, in this case, we used Hadamard masks of the resolution, 64×64, requiring 4096 measurements (with a runtime of ~4 h) to reconstruct our images. This is in contrast to our Hermite–Gauss basis set, which required significantly fewer modes, approximately an order of magnitude less (324 modes were used for the step and chess objects and 484 modes for the repeating chess object, (with a runtime of ~30–40 min), to achieve the same image reconstruction fidelity when employing our modal filtering technique.

To demonstrate the degree to which the modal filtering technique provides near-perfect reconstruction results, we determine the fidelity of our reconstruction for increasing filtering thresholds from 5% filtering up to 90% filtering, the results of which are shown in Figure 10 for the step and chess objects. This fidelity is computed as the normalized overlap between the experimental image, $I(x,y)$ and the ground truth image (or object), $O(x,y)$: $\frac{\sum O(x,y) I^*(x,y)}{\sqrt{\sum |O(x,y) I^*(x,y)|^2}}$. The fidelity measure is also used to determine the optimal threshold value that can be chosen. We see in Figure 10 that the fidelity of our reconstruction reaches a maximum for the Hermite–Gauss modes at a lower threshold, while the Hadamard set reaches the same maximum at higher thresholds in both cases. This could be attributed to the Hermite-Gauss reconstruction utilizing fewer modes, minimizing the number of lower-order modal contributions to filter out. This highlights

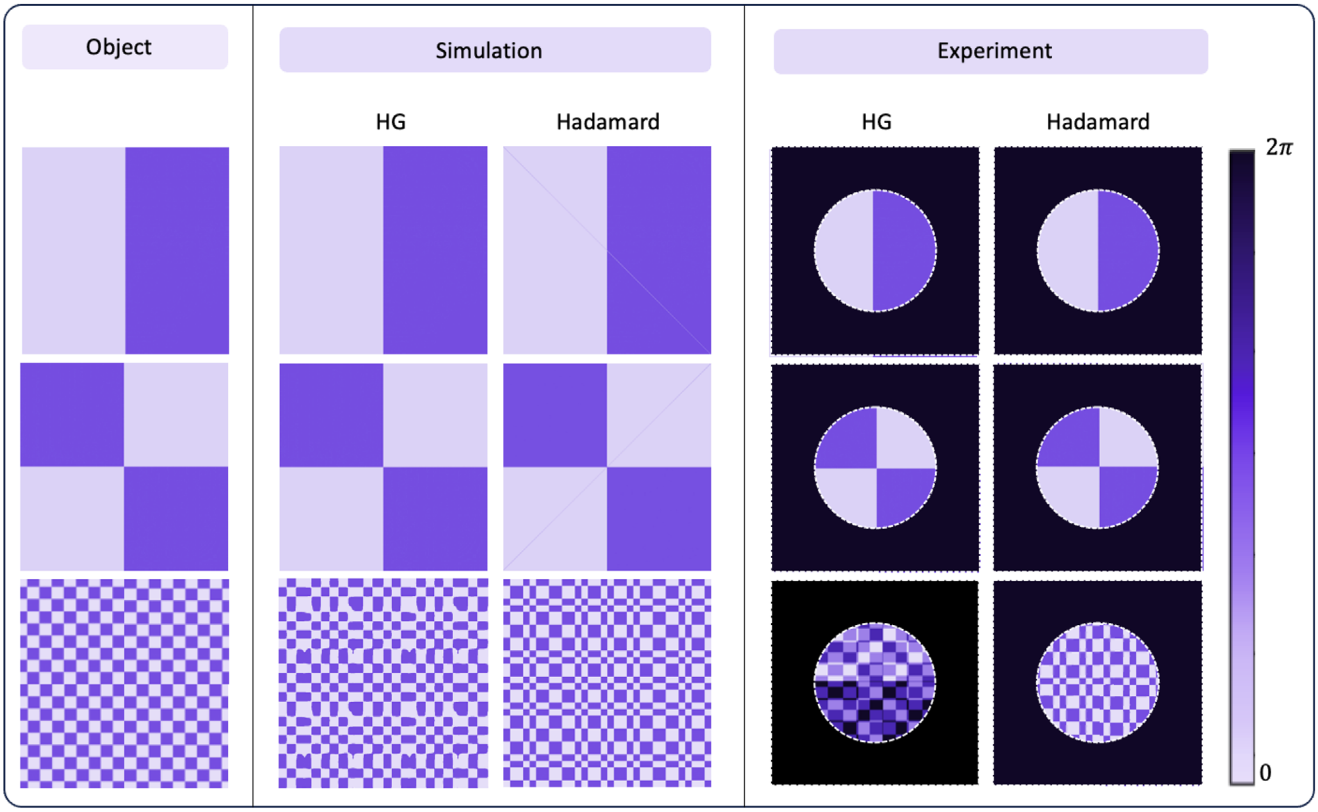

Figure 7. Near-perfect image reconstruction results achieved by employing modal sparsity in the imaging of phase-only objects. The first column illustrates the digital objects used. The second column shows a perfect simulation of the phase-only image reconstruction employing modal sparsity for HG and Hadamard modes, respectively. The third column shows the corresponding experimental perfectly reconstructed images employing modal sparsity.

an advantage of the Hermite–Gauss reconstruction set, suggesting that high-fidelity reconstruction can be achieved with fewer measurements and lower-modal filtering thresholds in the case of objects with Cartesian symmetry.

In **Figure 11**, the normalized modal power contributions for each of the HG modes used to reconstruct the repeating chess object are shown, exhibiting power peaks for specific modes. Again, we see that these modes have the largest overlap with our object and by filtering out the lower power contributions, we reveal higher-quality reconstructions of our object. Our initial noisy, raw experimental reconstruction is shown on the right, where it is enhanced to higher quality through increased modal filtering. From

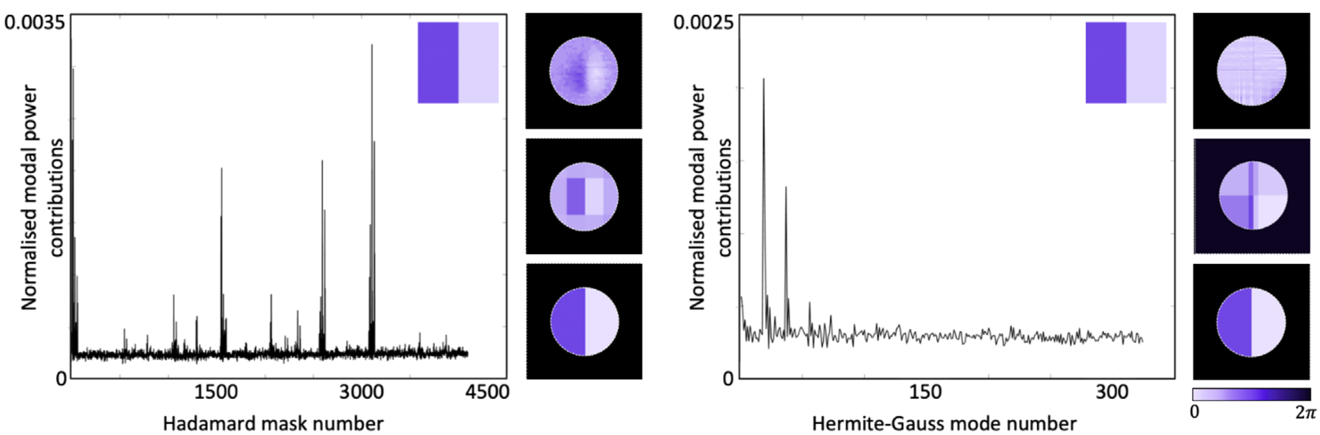

Figure 8. Normalized modal power contributions in the reconstruction of a phase-step using both Hadamard and Hermite–Gauss modes. The graphs show the normalized modal power contributions for each of the different modes while the side panels show the image reconstructions after satisfying three conditions. From top to bottom: no modal filtering, 50% modal filtering and 90% modal filtering.

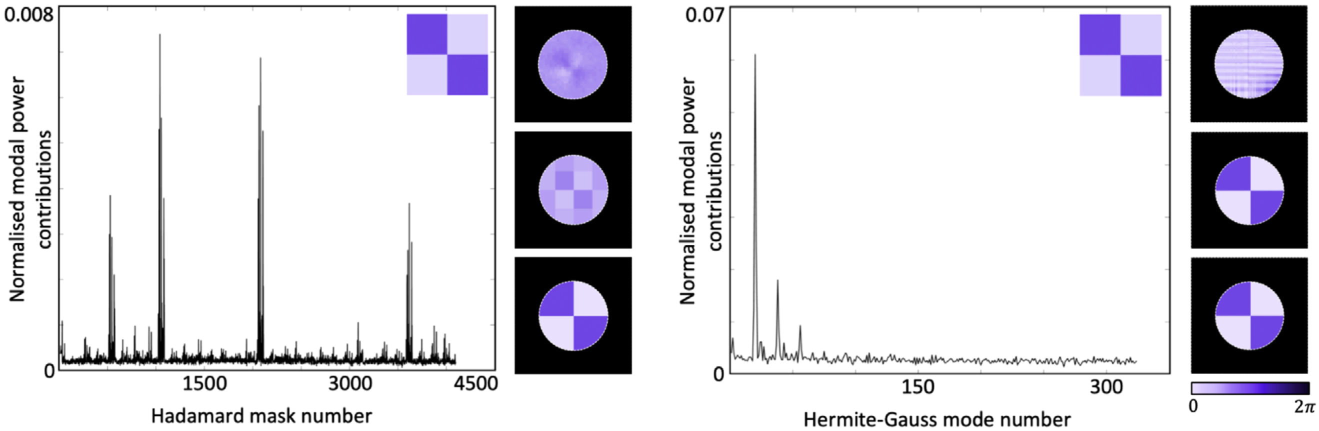

Figure 9. Normalized modal power contributions in the reconstruction of a phase chess board pattern using both Hadamard and Hermite–Gauss modes. The graphs show the normalized modal power contributions for each of the different modes while the side panels show the image reconstructions after satisfying three conditions. From top to bottom: no modal filtering, 50% modal filtering and 90% modal filtering.

top to bottom, we begin with no modal filtering, where considering all modal contributions in the reconstruction process yields an image with no distinct object present. With 50% modal filtering, noise from lower-order contributions is reduced, revealing a blurry phase pattern. Finally, 90% modal filtering reveals a clear repeating chess pattern.

It is important to note that the modal filtering thresholds are influenced by the noise level in the coincidence data. If the noise is uniform across the data, the thresholds remain unaffected, as all modes are equally impacted. However, noise is typically non-uniform, and as such, a fidelity measure can be used to identify the optimal threshold value as outlined above. We point out too that some knowledge of the object or SPDC size is useful in determining mode orders that can be ignored, since larger mode orders implies larger beams, although in principle this information can be deduced by noting the low counts at a threshold mode order.

5. Discussion

We have shown the advantage of the phase-only spatial mode approach to reconstruct phase objects without any interferometry. In this context, despite computational and technological advances, optical phase imaging has progressed slowly due to its experimental complexity.[59] Recent phase retrieval techniques using modern cameras include quantum-correlation enabled Fourier ptychography[60] and polarization-enabled holography,[61,62] however, these methods require single-photon cameras, which are expensive and have limited spectral sensitivity. An alternative phase retrieval approach using 2D projective masks has been shown with an interference-free effect,[51] reducing the number of measured variables required to extract phase information. However, this approach requires two different intensity values to extract the phase resulting in longer image acquisition times. By utilizing phase-only spatial modes as the

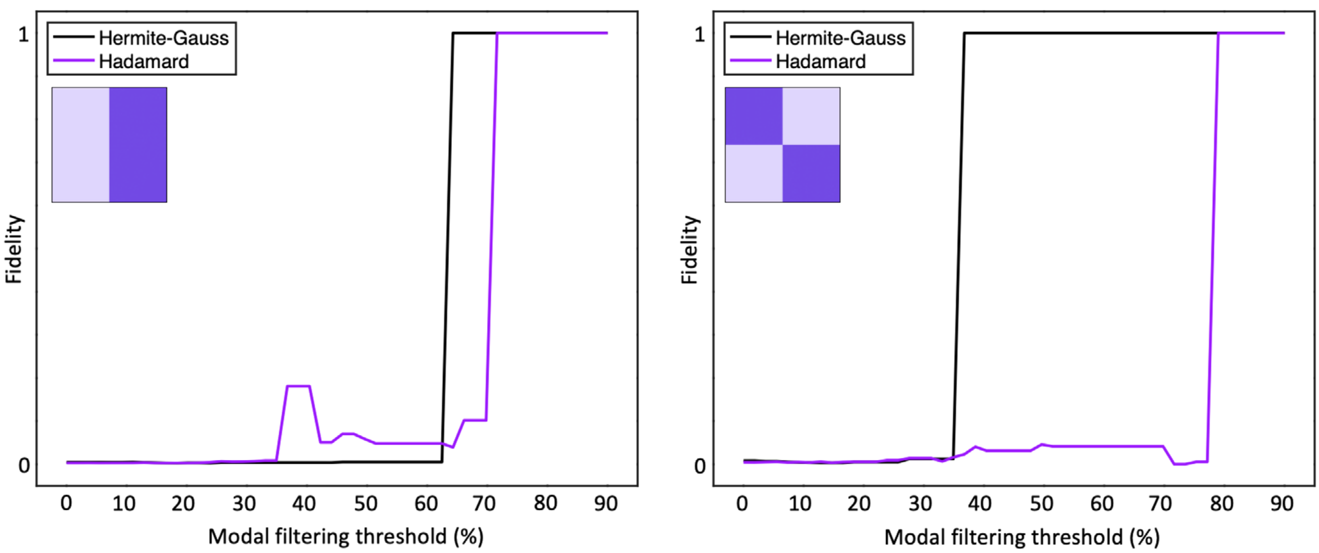

Figure 10. Reconstructed image fidelity for increasing modal filtering thresholds for the Hadamard and Hermite–Gauss basis sets for the step and chess objects, shown as insets.

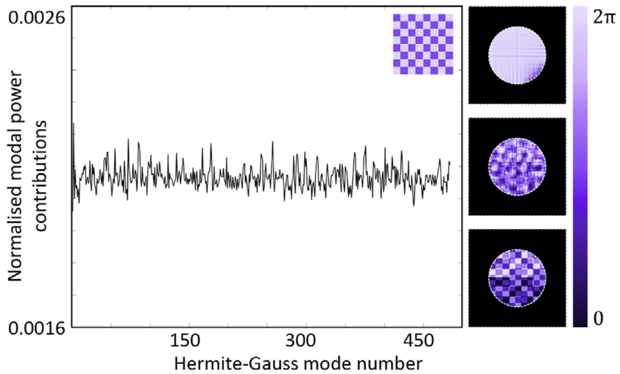

Figure 11. Normalized modal power contributions in the reconstruction of a repeating phase chessboard pattern (similar to that of squamous epithelium) using Hermite–Gauss modes. The panel on the right shows the image reconstructions after satisfying three conditions. From top to bottom: no modal filtering, 50% modal filtering and 90% modal filtering.

scanning basis, phase objects are reconstructed by a single intensity measurement with efficient phase-only masks. This method demonstrates robustness even when applied to complex objects as shown in Figure 6. However, its reconstruction performance depends significantly on the choice of the modal basis and consequently the number of required measurements. As object complexity increases, more measurements are needed to resolve intricate features, but selecting a modal basis that aligns with the object's symmetry – such as Cartesian for grid-like patterns or spiral for rotational features – can significantly enhance efficiency. This ensures that the method extracts maximum spatial information per measurement, maintaining feasibility even for more intricate structures. However, as we see in Figure 6b, certain experimental limitations can impede the accurate reconstruction of complex objects. These include resolution constraints imposed by the entanglement source, which limit the ability to resolve features smaller than the correlation width. This constraint arises from factors such as the characteristics of the SPDC source (e.g., crystal size, pump beam waist) and the design of the imaging and magnification system used to project onto the SLMs, as is evident in the reconstruction of the letter "H" in Figure 6b. Additionally, the inherently low efficiency of SPDC and the unequal detection probabilities of different spatial modes can lead to challenges in reconstructing complex objects. In such cases, the need for higher-order modes (which have lower detection efficiencies) or a large number of measurements further contributes to the inefficiency of object reconstruction.

Importantly in quantum ghost imaging, if the ultimate goal is to apply quantum ghost imaging to light-sensitive structures, a detector that quickly detects objects based on their symmetries and repeating patterns could be useful in several scenarios for imaging biological samples. For example, in cell biology, detecting cellular organization and polarity is essential for understanding how cells interact with their environment and maintain their functions. A detector capable of quickly identifying symmetrical patterns could aid in the analysis of cell division processes, where symmetry and asymmetry play critical roles in ensuring proper cell replication and differentiation. This could lead to advances in understanding diseases like cancer, where cell division rates are often accelerated and uncontrollable.[63] In this paper, the repeating chess object was selected due to its similarity to the structure of squamous epithelial cells, flat cells found throughout the body. Overproduction of these cells in the epidermis can indicate a type of skin cancer.[64] Moreover, for tissue analysis, the detection of regular patterns in tissue structures can help in identifying normal versus abnormal tissue organization. Rapid identification of these patterns could improve diagnostic techniques, particularly in pathology, where the assessment of tissue samples is key to diagnosing diseases. The ability to detect abnormalities in tissue organization could also be beneficial in monitoring disease progression or the effectiveness of treatments. Overall, such a detector could significantly accelerate biological analysis processes, providing real-time feedback in various biological research applications. This would not only improve efficiency but also enhance the accuracy and reliability of measurements, leading to advancements in multiple fields.

6. Conclusion

In conclusion, we have shown that the application of spatial modes in quantum ghost imaging yields high-resolution reconstructions of phase objects, with an order of magnitude less projections than using a pixel basis. By way of example, we have demonstrated the retrieval of the phase of the step, chess and repeating chess objects using phase-only Hermite–Gauss modes. We show that the HG phase-only masks used in our experiment comprise a non-orthogonal set, where a degree of orthogonality is preserved by considering the Gaussian envelope in this representation. Specifically, we show that when the image reconstruction data is modally sparse, filtering out lower-order contributions improves the fidelity of the reconstruction at a fraction of the measurements required for a general image reconstruction. Our approach introduces the notion of spatial modes as a basis for quantum imaging, and can easily be extended to other symmetries by appropriate basis choice. Finally, we note that although our objective here was imaging, the work can immediately be translated to quantum sensing without any significant changes in concept.

Acknowledgements

F.N. would like to acknowledge the financial support received from the CSIR under the HCD-IBS scholarship scheme. All authors acknowledge funding from SA QuTI.

Conflict of Interest

The authors declare no conflict of interest.

Data Availability Statement

The data that support the findings of this study are available from the corresponding author upon reasonable request.

Keywords

ghost imaging, quantum ghost imaging, spatial modes, structured light

Received: November 1, 2024
Revised: December 10, 2024
Published online: January 6, 2025

[1] Y. Shih, *IEEE J. Sel. Top. Quantum Electron.* **2007**, *13*, 1016.
[2] P.-A. Moreau, E. Toninelli, P. A. Morris, R. S. Aspden, T. Gregory, G. Spalding, R. W. Boyd, M. J. Padgett, *Opt. Express* **2018**, *26*, 7528.
[3] J. H. Shapiro, R. W. Boyd, *The Physics of Ghost Imaging*, vol. *11*, Springer, Berlin **2012**.
[4] M. J. Padgett, R. W. Boyd, *Philos. Trans. R. Soc., A* **2017**, *375*, 2099.
[5] C. Moodley, B. Sephton, V. Rodríguez-Fajardo, A. Forbes, *Sci. Rep.* **2021**, *11*, 1.
[6] C. Moodley, A. Forbes, *Laser Photonics Rev.* **2024**, 2300939.
[7] S. Vernekar, J. Xavier, *Quant. Beam Sci.* **2024**, *8*, 19.
[8] H. Defienne, W. P. Bowen, M. Chekhova, G. B. Lemos, D. Oron, S. Ramelow, N. Treps, D. Faccio, *Nat. Photonics* **2024**, *18*, 1024.
[9] N. Bornman, M. Agnew, F. Zhu, A. Vallés, A. Forbes, J. Leach, *npj Quantum Inf.* **2019**, *5*, 1.
[10] N. Bornman, S. Prabhakar, A. Vallés, J. Leach, A. Forbes, *New J. Phys.* **2019**, *21*, 073044.
[11] C. Pitsch, D. Walter, L. Gasparini, H. Bürsing, M. Eichhorn, *Appl. Opt.* **2023**, *62*, 6275.
[12] A. Gatti, E. Brambilla, L. Lugiato, *Progr. Optics* **2008**, *51*, 251.
[13] E. Baleine, A. Dogariu, G. S. Agarwal, *Opt. Lett.* **2006**, *31*, 2124.
[14] R. Weissleder, *Nat. Biotechnol.* **2001**, *19*, 316.
[15] Y. Zhang, Z. He, X. Tong, D. C. Garrett, R. Cao, L. V. Wang, *Sci. Adv.* **2024**, *10*, eadk1495.
[16] R. S. Aspden, N. R. Gemmell, P. A. Morris, D. S. Tasca, L. Mertens, M. G. Tanner, R. A. Kirkwood, A. Ruggeri, A. Tosi, R. W. Boyd, G. S. Buller, R. H. Hadfield, M. J. Padgett, *Optica* **2015**, *2*, 1049.
[17] T. B. Pittman, Y. H. Shih, D. V. Strekalov, A. V. Sergienko, *Phys. Rev. A* **1995**, *52*, 5.
[18] M. F. Duarte, M. A. Davenport, D. Takhar, J. N. Laska, T. Sun, K. F. Kelly, R. G. Baraniuk, *IEEE Signal Proc. Mag.* **2008**, *25*, 83.
[19] C. Moodley, A. Forbes, *JOSA B* **2023**, *40*, 3073.
[20] S. D. Johnson, P. A. Moreau, T. Gregory, M. J. Padgett, *Appl. Phys. Lett.* **2020**, *116*, 260504.
[21] P. Zerom, K. W. C. Chan, J. C. Howell, R. W. Boyd, *Phys. Rev. A: At., Mol., Opt. Phys.* **2011**, *84*, 3.
[22] V. Rodríguez-Fajardo, J. Pinnell, A. Forbes, *J. Mod. Opt.* **2020**, *0*, 1.
[23] C. Moodley, A. Forbes, *Sci. Rep.* **2022**, *12*, 10346.
[24] N. Bhusal, M. Hong, A. Miller, M. A. Quiroz-Juárez, R. d. J. León-Montiel, C. You, O. S. Maga na-Loaiza, *npj Quantum Inf.* **2022**, *8*, 83.
[25] P. A. Morris, R. S. Aspden, J. E. Bell, R. W. Boyd, M. J. Padgett, *Nat. Commun.* **2015**, *6*, 1.
[26] W. Zhang, X. Qiu, D. Zhang, L. Chen, *Laser Photonics Rev.* **2023**, *17*, 2200865.
[27] S. Johnson, J. Rarity, M. Padgett, *Sci. Rep.* **2024**, *14*, 11579.
[28] A. Forbes, M. De Oliveira, M. R. Dennis, *Nat. Photonics* **2021**, *15*, 253.
[29] J. Chen, C. Wan, Q. Zhan, *Adv. Photonics* **2021**, *3*, 064001.
[30] A. H. Dorrah, N. A. Rubin, M. Tamagnone, A. Zaidi, F. Capasso, *Nat. Commun.* **2021**, *12*, 6249.
[31] A. H. Dorrah, F. Capasso, *Science* **2022**, *376*, eabi6860.
[32] Q. Zhan, *Adv. Opt. Photonics* **2024**, *16*, 163.
[33] Z. Wan, H. Wang, Q. Liu, X. Fu, Y. Shen, *ACS Photonics* **2023**, *10*, 2149.
[34] J. Pinnell, I. Nape, B. Sephton, M. A. Cox, V. Rodríguez-Fajardo, A. Forbes, *JOSA A* **2020**, *37*, C146.
[35] M. Piccardo, M. de Oliveira, A. Toma, V. Aglieri, A. Forbes, A. Ambrosio, *Nat. Photonics* **2022**, *16*, 359.
[36] G.-k. Fu, J. Chen, G.-z. Qi, Y. Wu, X. Zhang, H.-l. Wang, Y. Shi, C.-l. Zhao, S.-z. Jin, *Opt. Express* **2023**, *31*, 1442.
[37] R. Wu, J. Chen, Y. Zhang, Y. Zhang, K. Zhao, Y. Li, Y. Shi, C. Zhao, R. Hao, S. Jin, *J. Lightwave Technol.* **2021**, *40*, 2008.
[38] S. Saito, *Front. Phys.* **2023**, *11*, 1225346.
[39] A. Bisht, N. Murillo, R. Vyas, S. Singh, *J. Opt. Soc. Am. A* **2024**, *41*, 2023.
[40] I. Nape, B. Sephton, P. Ornelas, C. Moodley, A. Forbes, *APL Photonics* **2023**, *8*, 5.
[41] C. Schiano, B. Sephton, R. Aiello, F. Graffitti, N. Lal, A. Chiuri, S. Santoro, L. S. Amato, L. Marrucci, C. de Lisio, V. D'Ambrosio, *Sci. Adv.* **2024**, *10*, eadm9278.
[42] D. Halevi, B. Lubotzky, K. Sulimany, E. G. Bowes, J. A. Hollingsworth, Y. Bromberg, R. Rapaport, *Optica Quant.* **2024**, *2*, 351.
[43] R. Shekel, O. Lib, Y. Bromberg, *Optica Quant.* **2024**, *2*, 303.
[44] Y. Shen, C. Rosales-Guzmán, *Laser Photonics Rev.* **2022**, *16*, 2100533.
[45] C. Schulze, D. Naidoo, D. Flamm, O. A. Schmidt, A. Forbes, M. Duparré, *Opt. Express* **2012**, *20*, 19714.
[46] J. Ma, D. Wei, L. Wang, Y. Zhang, M. Xiao, *Osa Continuum* **2021**, *4*, 1396.
[47] V. Rodríguez-Fajardo, A. Forbes, *Phys. Rev. Appl.* **2022**, *18*, 064068.
[48] M. Paúr, B. Stoklasa, Z. Hradil, L. L. Sánchez-Soto, J. Rehacek, *Optica* **2016**, *3*, 1144.
[49] P. Boucher, C. Fabre, G. Labroille, N. Treps, *Optica* **2020**, *7*, 1621.
[50] F. Grenapin, D. Paneru, A. D'Errico, V. Grillo, G. Leuchs, E. Karimi, *Phys. Rev. Appl.* **2023**, *20*, 024077.
[51] B. Sephton, I. Nape, C. Moodley, J. Francis, A. Forbes, *Optica* **2023**, *10*, 286.
[52] L. Chen, J. Lei, J. Romero, *Light: Sci. Appl.* **2014**, *3*, e153.
[53] B. Jack, J. Leach, J. Romero, S. Franke-Arnold, M. Ritsch-Marte, S. Barnett, M. Padgett, *Phys. Rev. Lett.* **2009**, *103*, 083602.
[54] C. Schulze, A. Dudley, D. Flamm, M. Duparre, A. Forbes, *New J. Phys.* **2013**, *15*, 073025.
[55] H. Wang, S. Han, M. I. Kolobov, *Opt. Express* **2012**, *20*, 23235.
[56] K. Piché, J. Leach, A. S. Johnson, J. Z. Salvail, M. I. Kolobov, R. W. Boyd, *Opt. Express* **2012**, *20*, 26424.
[57] J. Schneeloch, J. C. Howell, *J. Opt.* **2016**, *18*, 053501.
[58] F. Devaux, E. Lantz, *Eur. Phys. J. D* **2000**, *8*, 117.
[59] Z. Chen, J. Cheng, H. Wu, *Sensors* **2023**, *23*, 9405.
[60] T. Aidukas, P. C. Konda, A. R. Harvey, M. J. Padgett, P.-A. Moreau, *Sci. Rep.* **2019**, *9*, 1.
[61] B. Ndagano, H. Defienne, D. Branford, Y. D. Shah, A. Lyons, N. Westerberg, E. M. Gauger, D. Faccio, *Nat. Photonics* **2022**, *16*, 384.
[62] Y. Zhang, A. Sit, F. Bouchard, H. Larocque, F. Grenapin, E. Cohen, A. C. Elitzur, J. L. Harden, R. W. Boyd, E. Karimi, *Opt. Express* **2019**, *27*, 2212.
[63] D. Hanahan, R. A. Weinberg, *Cell* **2011**, *144*, 646.
[64] T. D. Pop, Z. Diaconeasa, *Int. J. Mol. Sci.* **2021**, *22*, 9707.